CD8+ lymphocytes modulate Zika virus dynamics and tissue dissemination and orchestrate antiviral immunity

Blake Schouest[1,2], Marissa Fahlberg[3], Elizabeth A. Scheef[2], Matthew J. Ward[4], Kyra Headrick[4], Dawn M. Szeltner[2], Robert V. Blair[5], Margaret H. Gilbert[6], Lara A. Doyle-Meyers[6], Victoria W. Danner[6], Myrna C. Bonaldo[7], Dawn M. Wesson[4], Antonito T. Panganiban[2,8], Nicholas J. Maness[2,8]*

[1]Biomedical Sciences Training Program, Tulane University School of Medicine, New Orleans, LA, USA

[2]Division of Microbiology, Tulane National Primate Research Center, Covington, LA, USA

[3]Division of Immunology, Tulane National Primate Research Center, Covington, LA, USA

[4]School of Public Health and Tropical Medicine, Tulane University, New Orleans, LA, USA

[5]Division of Comparative Pathology, Tulane National Primate Research Center, Covington, LA, USA

[6]Division of Veterinary Medicine, Tulane National Primate Research Center, Covington, LA, USA

[7]Laboratório de Biologia Molecular de Flavivírus, Instituto Oswaldo Cruz, Fiocruz, Rio de Janeiro, RJ, Brazil

[8]Department of Microbiology and Immunology, Tulane University School of Medicine, New Orleans, LA, USA

*Corresponding author, Nicholas J Maness, nmaness@tulane.edu

Abstract

CD8+ lymphocytes are critically important in the control of viral infections, but their roles in acute Zika virus (ZIKV) infection remain incompletely explored in a model sufficiently similar to humans immunologically. Here, we use CD8+ lymphocyte depletion to dissect acute immune responses in adult male rhesus and cynomolgus macaques infected with ZIKV. CD8 depletion delayed serum viremia and dysregulated patterns of innate immune cell homing and monocyte-driven transcriptional responses in the blood. CD8-depleted macaques also showed evidence of compensatory adaptive immune responses, with elevated Th1 activity and persistence of neutralizing antibodies beyond the clearance of serum viremia. The absence of CD8+ lymphocytes increased viral burdens in lymphatic tissues, semen, and cerebrospinal fluid, and neural lesions were also evident in both CD8-depleted rhesus macaques. Together, these data support a role for CD8+ lymphocytes in the control of ZIKV dissemination and in maintaining immune regulation during acute infection of nonhuman primates.

Introduction

ZIKV has been a known pathogen for over half a century (Dick et al., 1952), but severe manifestations of the disease were not directly associated with the virus for most of its history. Although recent outbreaks of ZIKV in the Western hemisphere are notorious for neurological complications including congenital Zika syndrome (CZS) and Guillain-Barré syndrome (GBS), most cases remain asymptomatic, and when symptoms arise, they are usually mild and self-limiting (Plourde and Bloch, 2016). Differential immune responses to ZIKV infection may dictate the severity of accompanying diseases and underlie clinical outcomes.

As the immunological correlates of protection against ZIKV are beginning to be explored, the CD8 T cell response is emerging as an important mediator of viral control, as is true with other flaviviruses (Slon Campos et al., 2018). Studies in mice have identified CD8 T cell responses to ZIKV infection, but the induction of ZIKV-associated pathology in these models requires deficiency in type-I interferon (IFN) signaling (Elong Ngono et al., 2017; Huang et al., 2017), which is not representative of natural ZIKV infection in humans. This is perhaps an unavoidable caveat, as ZIKV is incapable of antagonizing type-I IFN signaling in mice as it does in humans due to a lack of recognition of murine STAT2 by ZIKV NS5 (Grant et al., 2016). Disrupting IFN-I signaling, either genetically or through antibody blockade is, therefore, necessary to recapitulate ZIKV neurotropism in mouse models. Importantly, these studies have described dual protective and deleterious effects of CD8 T cell responses in ZIKV infected mice. While CD8+ lymphocyte infiltration appears to reduce viral burdens in the brain, spinal cord and lymphatic tissue (Elong Ngono et al., 2017; Huang et al., 2017), under certain circumstances, CD8+ influx may also promote immunopathology, evidenced by neural damage and paralysis (Jurado et al., 2018). However, these findings have yet to be replicated in a model sufficiently similar to humans genetically and immunologically. Given the recent development of rhesus (Coffey et al., 2017; Dudley et al., 2016; Dudley et al., 2018; Magnani et al., 2018a; Osuna et al., 2016a) and cynomolgus (Koide et al., 2016; Osuna et al., 2016a) macaque models of ZIKV infection, we sought to explore the role of CD8+ lymphocytes in acute ZIKV infection by way of CD8+ lymphocyte depletion. CD8+ depletion is a well-established immune manipulation in nonhuman primates (Schmitz et al., 1999) and is thus a plausible approach to gauge how the absence of CD8+ cells impacts acute viremia and potentially modulates adaptive responses.

In the present study, we infected four adult male rhesus macaques and five adult male cynomolgus macaques with a minimally passaged Brazilian ZIKV strain. Prior to infection, two animals of each species were depleted of CD8+ lymphocytes, including CD8 T cells and natural killer (NK) cells. The absence of CD8+ lymphocytes resulted in striking virus-response patterns that were not evident in nondepleted macaques, including delayed serum viremia, enhanced viral dissemination to peripheral tissues, and global repression of antiviral gene transcription. CD8-depleted rhesus macaques also manifested brainstem lesions that were characterized by increased inflammation. Finally, the absence of CD8+ lymphocytes appeared to alter patterns of monocyte expansion and activation and induce compensatory adaptive responses, characterized by enhanced Th1 phenotypes and prolonged neutralizing antibody production.

Methods

Animal experiments

The four adult male Indian origin rhesus macaques (*Macaca mulatta*) and five adult male cynomolgus macaques (*Macaca fascicularis*) utilized in this study were housed at the Tulane

National Primate Research Center (TNPRC). The TNPRC is fully accredited by AAALAC International (Association for the Assessment and Accreditation of Laboratory Animal Care), Animal Welfare Assurance No. A3180-01. Animals were cared for in accordance with the NRC Guide for the Care and Use of Laboratory Animals and the Animal Welfare Act Animal experiments were approved by the Institutional Animal Care and Use Committee of Tulane University (protocol P0367).

Two rhesus macaques (R25671 and R64357) and two cynomolgus macaques (C78777 and C18942) were depleted of CD8+ lymphocytes by administration of the anti-CD8α antibody MT807R1 (NHP Reagent Resource; https://www.nhpreagents.org) (Schmitz et al., 1999). The initial subcutaneous administration of 10 mg/kg at 14 days pre-infection was followed by three intravenous administrations of 5 mg/kg at 11, 7, and 5 days pre-infection, as per the distributor's protocol. C84545 was treated with the irrelevant control antibody anti-desmipramine (NHP Reagent Resource; https://www.nhpreagents.org) at the same dosages and time intervals pre-infection. All animals were subcutaneously infected with 10^4 PFU of a Brazilian ZIKV isolate (Bonaldo et al., 2016) at 0 days post-infection (dpi) (Fig. 1a). As part of a previous study, C46456 (nondepleted cynomolgus macaque) was splenectomized 9 months and 19 days prior to inoculation with ZIKV. For data comparison, we included viral loads and complete blood count (CBC) data from a previous cohort of 4 non-pregnant female rhesus macaques (R32835, R24547, R25508, R22624) that were similarly infected with the same dose of the same Brazilian ZIKV isolate that was used in this study (Supplementary Figs. 2a-e).

Whole blood, cerebrospinal fluid (CSF), and semen were obtained from animals at the indicated timepoints (Fig. 1a). Peripheral blood mononuclear cells (PBMCs) were isolated from the blood of rhesus macaques using SepMate tubes (Stemcell Technologies) according to the manufacturer's protocol or from the blood of cynomolgus macaques using Lymphoprep (Stemcell Technologies) for standard density gradient centrifugation. At necropsy, the indicated tissues were collected and snap-frozen.

Virus quantification

Viral RNA was extracted from serum and CSF using the High Pure Viral RNA Kit (Roche). Semen, as well as the indicated lymphoid, reproductive, GI, and neural tissues were homogenized in Qiazol (Qiagen) using either disposable tissue grinders (Fisherbrand) or a TissueRuptor (Qiagen), and RNA was isolated using the RNeasy Lipid Tissue Mini Kit (Qiagen). Viral RNA from body fluids and tissues was quantified using qRT-PCR as described previously (Magnani et al., 2018b).

Antiviral gene expression assays

2.5 ml whole blood was drawn from each animal at 0, 1, 3, and 15 dpi into PAXgene blood RNA tubes (PreAnalytiX) and equilibrated to -80˚C as per the manufacturer's protocol. RNA was extracted from blood samples using the PAXgene blood RNA kit (PreAnalytiX), and cDNA was synthesized using the RT2 First Strand Kit (Qiagen). Transcriptional profiles of immune signaling were generated using the nCounter NHP Immunology Panel of 770 macaque immune response genes (NanoString Technologies). In whole blood, transcriptional responses were assessed at 3 dpi relative to expression levels pre-infection using nSolver software v4.0 (NanoString Technologies). Fold change data were imported into Ingenuity Pathway Analysis (IPA) (Qiagen) to discern relevant signaling pathways and disease functions. Antiviral transcriptional responses were confirmed by way of qRT-PCR using a rhesus macaque RT2

Profiler PCR Array (Qiagen). Responses within each species and treatment group were analyzed together to identify expression levels at the indicated timepoints relative to pre-infection. Heatmaps of gene expression and disease-related pathways were generated using Morpheus (https://software.broadinstitute.org/Morpheus). Principal component analysis (PCA) of antiviral gene expression was performed using ClustVis (Metsalu and Vilo, 2015).

To identify cell populations contributing to antiviral signaling in blood, the CD14 and CD8 MicroBead kits (Miltenyi Biotec) were used to sort CD14+ monocytes and CD8+ lymphocytes from the PBMCs of the indicated animals at peak transcriptional activity (3 dpi). RNA was isolated from cell fractions using the RNeasy Mini Kit (Qiagen), and cDNA was synthesized using the RT2 First Strand Kit (Qiagen). Transcriptional profiling was performed using the nCounter NHP Immunology Panel (NanoString) and verified by RT2 qPCR Primer Assays (Qiagen) for ISG15, OAS2, and DDX58.

To characterize antiviral signaling in myeloid cells, PBMCs were isolated from the whole blood of ZIKV-naïve colony rhesus macaques as described above, and the CD14 MicroBead kit (Miltenyi Biotec) was used to isolate monocytes. For the co-culture assay, monocytes were incubated in the presence or absence of autologous CD8+ cells and/or ZIKV in a 96-well U-bottom plate with 50,000 cells of each type plated per well for the indicated timepoints. qPCR for ISG15 and OAS2 was performed as described above. For antiviral gene screening in monocyte-derived macrophages (MDMs), monocytes were cultured at 1×10^6 cells/ml in RPMI-1640 medium supplemented with 1% human AB serum (Sigma), 20 ng/ml M-CSF (Peprotech), 1% L-glutamine, and 1% penicillin/streptomycin. After 7 days of culture, monocytes were sufficiently differentiated into MDMs and were either infected with the same Brazilian ZIKV isolate described above or left uninfected. At 24 hpi, RNA was extracted using the RNeasy Mini Kit (Qiagen), cDNA was synthesized using the RT2 First Strand Kit (Qiagen), and transcriptional signaling was assessed using the rhesus macaque antiviral response RT2 Profiler PCR Array (Qiagen). Antiviral gene expression in ZIKV-infected monocyte-derived macrophages (MDMs) was calculated relative to uninfected controls.

Flow cytometry and gating strategy

For absolute lymphocyte counts, whole blood was stained within 2 hours of blood draw for the surface markers CD45 (PerCP; DO58-1283; BD Biosciences), CD3 (FITC; SP34; BD Biosciences), CD4 (APC; L200; BD Biosciences), and CD8 (V500; SK1; BD Biosciences). Flow cytometry was performed on a BD FACSVerse instrument, and absolute counts were calculated using FACS Suite software.

For immunophenotyping, PBMCs from the indicated timepoints were thawed, washed, and stained using Live/Dead Fixable Aqua Dead Cell Stain Kit (Invitrogen). PBMCs were then stained for the surface markers CD16 (AL488; 3G8; BioLegend), CD169 (PE; 7-239; BioLegend), CD28 (PECF594; CD28.2; BD Biosciences), CD95 (PCP-Cy5.5; DX2; BioLegend), CD3 (PE-Cy7; SP34-2; BD Biosciences), CD8 (PacBlue; SK1; BioLegend), CD14 (BV605; M5E2; BD Biosciences), HLA-DR (BV650; L243; BioLegend), NKG2A (APC; Z199; Beckman Coulter), and CD4 (APC-H7; L200; BD Biosciences). Cells were subsequently fixed in FluoroFix buffer (BioLegend), permeabilized using Perm/Wash buffer (BioLegend), and stained intracellularly for CD69 (BV711; FN50; BD Biosciences) and Ki67 (AL700; B56; BD Biosciences). Flow cytometry was performed on a BD LSRII instrument and data were analyzed using FlowJo (vX.10.4.2) and visual t-distributed stochastic neighbor embedding (viSNE)

167 (Cytobank) softwares. For viSNE analysis, live singlet monocytes (CD14+ and/or CD16+) or
168 live singlet CD3+ T cells were gated prior to downsampling at a minimum of 500 cells per
169 animal in FlowJo v. 10.5.3. Downsampled files for each animal were then concatenated by group
170 (i.e., species, dpi, and treatment condition). When the number of animals differed per group,
171 concatenated files were further downsampled to achieve an equal number of cells per group.
172 viSNE was conducted using Cytobank with the following settings: Perplexity = 30, Iterations =
173 1000, Theta = 0.5, Seed = random, Compensation = internal file. For the monocyte viSNE, the
174 following parameters were utilized in the run: Ki67, CD14, HLA-DR, CD69, CD95, CD14, and
175 CD169. For the CD3+ T cells viSNE, the following parameters were utilized in the run: Ki67,
176 CD4, HLA-DR, CD69, CD95, CD28, CD3, CD8.

177 For general immunophenotyping analysis, cytometry data were first gated for lymphocytes,
178 singlets, and live cells. NK cells were considered as CD8+/CD16+. CD4 T cells (CD3+/CD4+)
179 and CD8 T cells (CD3+/CD8+) were gated into naïve (CD28+/CD95-), central memory (CM)
180 (CD28+/CD95+), and effector memory (EM) (CD28-/CD95+) subsets. CD3- cells were divided
181 into B cells (DR+/CD14-/CD16-) and monocytes (classical, CD14++/CD16-; intermediate,
182 CD14+/CD16+; nonclassical, $CD14^{low}$/CD16+). Cell subsets were analyzed with respect to
183 frequency, proliferation (Ki67+) and activation (CD69+ or CD169+).

184 **Intracellular cytokine staining**
185 PBMCs from the indicated timepoints were thawed and rested overnight prior to stimulation with
186 peptide pools comprising ZIKV capsid (C), membrane (M), envelope (E), and nonstructural
187 protein 1 (NS1) (BEI Resources). On peptide stimulation, cells were also treated with brefeldin
188 A (BioLegend), GolgiStop (BD Biosciences), anti-CD28 (NHP Reagent Reference Program,
189 www.nhpreagents.org/), anti-CD49d (9F10; BioLegend), and anti-CD107a (AL700; H4A3; BD
190 Biosciences). 24 hours post-stimulation, cells were stained for the surface markers CD3 (PE-
191 Cy7; SP34-2; BD Biosciences), CD8 (PacBlue; SK1; BioLegend), and CD4 (APC-H7; L200;
192 BD Biosciences). Cells were also fixed and permeabilized as described above and stained
193 intracellularly for perforin (FITC; Pf-344; Mabtech), granzyme B (PE; GB12; Invitrogen), CD69
194 (PE-CF594; FN50; BD Biosciences), IL-2 (PCP-Cy5.5; MQ1-17H12; BD Biosciences), and
195 IFNγ (AL647; 4S.B3; BioLegend). Flow cytometry was performed on a BD LSRII instrument
196 and data were analyzed using FlowJo software (vX.10.4.2).

197 **Plaque reduction neutralization tests**
198 ZIKV plaque reduction neutralization tests (PRNTs) were conducted according to previously
199 published protocols (Lieberman et al., 2009; Ward et al., 2018). Briefly, ZIKV MEX-I-44
200 isolated in Tapachula, Mexico in 2016 was obtained from The University of Texas Medical
201 Branch, Galveston, TX and cultured to passage 8 in Vero cells. Serum specimens were incubated
202 for one hour at serial dilutions of 1:10, 1:20…1:320 with a previously frozen virus stock of
203 known plaque forming unit (PFU). Samples were then inoculated in duplicate onto a mono-layer
204 of Vero cells grown on 6-well plates and allowed to incubate for an additional hour. Infectious
205 material was then removed and replaced with a 1:1 mixture of Vero media and Avicel® before
206 being incubated for 4 days. To read plaques, the Avicel® layer was fixed with 10% neutral
207 buffered formalin. Finally, the formalin-Avicel® layer was removed and the monolayer was
208 stained with crystal violet, washed with tap water and allowed to dry before plaques were
209 counted manually.

210 Percent reduction in observed plaques and a PRNT90 cutoff were used for interpretation. A
211 PRNT90 titer is the dilution of a sample at which a 90% reduction in possible plaques is
212 observed. The maximum number of potential plaques was obtained for each run using a
213 corresponding back-titration and a linear model was fit to the observed number of plaques for
214 each dilution. A PRNT90 titer was derived for each sample using the linear model and the
215 equation for a straight line in the statistical program R (R Core Team, 2018). For samples that
216 were positive but above the resolution of the PRNT assay the value of the greatest number of
217 possible plaques for that run, as determined by the back titration, was assigned for each dilution
218 for use with the linear model.

219 **Histology**

220 Tissues samples collected at necropsy were fixed in Z-Fix (Anatech), embedded in paraffin and 5
221 μm thick sections were cut, adhered to charged glass slides, and either stained routinely with
222 hematoxylin and eosin or Prussian blue.

223 **Statistical analysis**

224 Statistical analysis was conducted using GraphPad Prism v6.07 (GraphPad Software). A Mann-
225 Whitney test was used to compare neutrophil-to-lymphocyte ratios (NLRs) among treatment
226 conditions (CD8-depleted versus nondepleted).

227 **Results**

228 **Delayed serum viremia and altered leukocyte kinetics**

229 CD8+ lymphocyte depletion commenced 14 days prior to ZIKV infection (Fig. 1a), and CD8 T
230 cells were undetectable in all depleted animals well before infection (Fig. 1b & Supplementary
231 Fig. 1a). To achieve CD8 depletion, we used the MT807R1 antibody (Schmitz et al., 1999) to
232 target CD8α, effectively depleting CD8 T cells (Fig. 1b & Supplementary Fig. 1a), CD8+/CD4+
233 double-positive T cells (Supplementary Fig. 1b), and NK cells (Fig. 1c) but not CD4 T cells
234 (Supplementary Fig. 1c) from the blood of all treated animals. As MT807R1 targets NK cells in
235 addition to CD8+ lymphocytes, any deficiency in host response following treatment with anti-
236 CD8α could indicate that either or both types of cells are important for acute control of ZIKV.
237 Flow cytometric analysis of NK cell frequency in nondepleted animals revealed expansion early
238 in infection (Fig. 1c). Intriguingly, the CD8-depleted macaque R64357 recovered CD8 T cells
239 and NK cells at later timepoints, between 15 and 21 days post-infection (dpi) (Figs. 1b-c).

240 Following subcutaneous inoculation with ZIKV, nondepleted animals and a single CD8-depleted
241 cynomolgus macaque experienced rapid serum viremia of 3-4.5 logs at 1 dpi (Fig. 1d), consistent
242 with previous reports of ZIKV in both rhesus and cynomolgus macaques (Dudley et al., 2016;
243 Koide et al., 2016; Osuna et al., 2016b). Strikingly, serum viremia in 3 of 4 CD8-depleted
244 macaques was delayed until 2 dpi, when viral RNA was higher than in nondepleted animals (Fig.
245 1d). Viremia was also delayed until 3 dpi in *C46456 (Fig. 1d), a nondepleted cynomolgus
246 macaque that had been previously splenectomized. Perhaps importantly, the spleen is a major
247 site of replication and spread of the related mosquito-borne flaviviruses dengue virus (DENV)
248 (Prestwood et al., 2012) and West Nile virus (WNV) (Bryan et al., 2018) and is also an immense
249 reservoir of monocytes (Swirski et al., 2009), which are permissive to ZIKV replication in
250 humans (Michlmayr et al., 2017) and macaques (O'Connor et al., 2018). The lack of a spleen in
251 *C46456 (nondepleted) might have precluded ZIKV replication in this important target organ,
252 thereby delaying viral kinetics.

253 By 7 dpi, serum viremia persisted in the CD8-depleted cynomolgus macaques in addition to the
254 mock-depleted control, while viremia was undetected in both nondepleted animals of the cohort
255 (Fig. 1d). For the remainder of the study, viral kinetics were similar among cohorts and treatment
256 conditions, peaking at 3 dpi and dropping to undetectable levels by 10 dpi and beyond (Fig. 1d).
257 This was again in exception to *C46456 (nondepleted), which showed a small viral rebound at
258 10 dpi. A previous cohort of female macaques infected with the identical strain of ZIKV
259 demonstrated similar patterns of serum viremia to those observed in nondepleted animals
260 (Supplementary Fig. 2a).

261 The previous female cohort also showed consistent patterns of innate immune cell recruitment in
262 the blood one day following ZIKV infection, summarized by the biomarker neutrophil-to-
263 lymphocyte ratio (NLR) (Faria et al., 2016). Patterns of leukocyte mobilization included a spike
264 in neutrophil frequency (Supplementary Fig. 2c) and a simultaneous drop in lymphocyte
265 frequency (Supplementary Fig. 2d), resulting in an elevated NLR at 1 dpi (Supplementary Fig.
266 2e). These findings were generally recapitulated in nondepleted animals but not in CD8-depleted
267 animals (Figs. 1e-f and Supplementary Figs. 2c-e), potentially linking NLR and acute serum
268 viremia, although the trend did not hold in the mock-depleted cynomolgus macaque C84545.
269 This association is strengthened by prototypical patterns of leukocyte homing in C78777 (Fig.
270 1e), the only CD8-depleted macaque with serum viremia at 1 dpi (Fig. 1d).

271 **Differential monocyte-driven transcriptional profiles**

272 To characterize immune responses that might be differentiating patterns of viremia and leukocyte
273 mobilization, we used the NanoString platform to quantify the expression of macaque immune-
274 related genes in whole blood. CD8-depleted and nondepleted animals showed highly divergent
275 profiles in genes related to IFNα signaling (Fig. 2a) and leukocyte homing (Supplementary Fig.
276 3a), resulting in the robust induction of disease-related pathways in nondepleted macaques that
277 failed to activate in animals lacking CD8+ lymphocytes (Supplementary Fig. 3b). To confirm the
278 transcriptional quiescence evident in CD8-depleted macaques, we used a quantitative real-time
279 PCR (qRT-PCR) array of 84 antiviral genes in the rhesus macaque genome. Consistent with the
280 NanoString results, nondepleted rhesus and cynomolgus macaques showed strong induction of
281 several RIG-I like receptors (RLRs) and type-I IFN stimulated genes (ISGs) at 3 dpi,
282 synchronous with peak serum viremia (Fig. 2b). The most highly induced genes include the
283 pattern recognition receptors *TLR3*, *DDX58* (also known as *RIG-I*), and *IFIH1* (also known as
284 *MDA5*), as well as the ISGs *ISG15*, *MX1*, and *OAS2*. Principal component analysis (PCA) of
285 antiviral signaling further discriminated the transcriptional phenotypes in CD8-depleted and
286 nondepleted animals (Fig. 2c). The induction of antiviral genes in nondepleted rhesus macaques
287 was highest at 3 dpi and was generally followed by a return to near-baseline expression by 15 dpi
288 (Supplementary Fig. 3c). In contrast to nondepleted animals, CD8-depleted macaques showed a
289 virtual absence of transcriptional responses in whole blood at all timepoints tested (Figs. 2a-b
290 and Supplementary Fig. 3d).

291 Although we suspected monocytes to be driving antiviral gene expression owing to their
292 susceptibility to ZIKV infection (Michlmayr et al., 2017; O'Connor et al., 2018), an important
293 caveat of probing whole blood is that the identity of the cell populations responding
294 transcriptionally is unknown. To resolve cell populations contributing to antiviral signaling in
295 blood, we sorted CD14+ monocytes from peripheral blood mononuclear cells (PBMCs) at 3 dpi
296 and profiled their expression of immune genes. Probe hybridization revealed selective antiviral
297 gene expression in the monocytes of a nondepleted macaque and showed that even purified and

298 sorted PBMCs from a CD8-depleted animal fail to establish transcriptional responses at peak
299 serum viremia (Fig. 2d). These findings were verified by qRT-PCR (Fig. 2e). Nonetheless, it
300 remained possible that the lack of a transcriptional response in CD8-depleted macaques could
301 have been attributed in part to an absence of otherwise responding NK cells. Sorting PBMCs
302 from a nondepleted rhesus macaque into CD8+ and CD8- fractions, we found similar levels of
303 gene induction in both populations, although expression was marginally higher in the CD8-
304 subset, and transcription of *DDX58* was almost exclusive to CD8- cells (Fig. 2f). Gene induction
305 in CD8+ cells indicates that NK cells may indeed contribute to antiviral signaling, but similar
306 transcriptional activation in the CD8- fraction affirms that the absence of transcriptional
307 activation in CD8-depleted animals was not simply the product of a lack of NK cells.

308 To further explore transcriptional responses to ZIKV in myeloid cells, we infected monocyte-
309 CD8 cell co-cultures *ex vivo* and compared antiviral gene expression to monocytes infected in
310 the absence of CD8+ cells, finding that the presence of CD8+ lymphocytes is important in
311 promoting transcriptional responses (Fig. 2g). We also cultured monocyte-derived macrophages
312 (MDMs) *in vitro*, infected the macrophages with ZIKV, and profiled antiviral gene expression
313 using qRT-PCR. We found an overlapping transcriptional fingerprint to those observed in the
314 blood of nondepleted rhesus and cynomolgus macaques at 3 dpi (Fig. 2h), suggesting that ZIKV-
315 permissive myeloid cells may be driving antiviral gene induction *in vivo*. Although cultured
316 MDMs exhibited higher induction of several TLR responsive genes (Fig. 2g), this difference
317 might be attributed to cell type.

318 **Altered monocyte activation and frequency**
319 Divergent transcriptional patterns in CD8-depleted and nondepleted macaques could be induced
320 by differentially responding monocytes, given that monocytes are known targets of ZIKV
321 infection (Lum et al., 2018; O'Connor et al., 2018) and contribute to antiviral signaling during
322 ZIKV infection (Lum et al., 2018). To interrogate the immunophenotypic effects of CD8
323 depletion, we developed a multicolor flow cytometry panel to track innate and adaptive immune
324 cells over time. The resulting data were highly dimensional, comprising a variety of surface
325 markers and sampling animals at multiple timepoints and with respect to different treatment
326 groups. To survey general immune responses over time, we used an adaptation of t-distributed
327 stochastic neighbor embedding (tSNE), viSNE (Amir et al., 2013).

328 In both rhesus and cynomolgus macaques, CD8 depletion dysregulated the kinetics of monocyte
329 activation as measured by CD169 (siglec-1) expression (Biesen et al., 2008; Hirsch et al., 2018;
330 York et al., 2007). Nondepleted rhesus and cynomolgus macaques showed early activation of
331 monocytes, peaking at 3 dpi and returning sharply to baseline by 14-15 dpi (Figs. 3a-c).
332 Upregulation of CD169 in nondepleted animals was affirmed at the RNA level (Fig. 2a).
333 Although patterns of CD169 induction were consistent in all monocyte subsets (Supplementary
334 Figs. 4a-c), viSNE analysis indicated that CD169 was most highly expressed on intermediate and
335 nonclassical monocytes in both cohorts (Figs. 3a-b). Contrasting nondepleted animals, CD8-
336 depleted rhesus and cynomolgus macaques showed less well-defined monocyte activation at 3
337 dpi, which was accompanied in rhesus macaques by prolonged monocyte activation beyond 15
338 dpi (Figs. 3a-c & Supplementary Figs. 4a-d). These findings were consistent transcriptionally, as
339 whole blood from CD8-depleted animals had muted expression of genes related to myeloid cell
340 activation (Fig. 3d). Monocyte subsets showed additional nuances in phenotype that appeared
341 dependent on CD8 depletion: In rhesus macaques, CD95 (Fas) was increased on classical
342 monocytes in CD8-depleted animals (Supplementary Fig. 4e) and on nonclassical monocytes in

343 nondepleted animals (Supplementary Fig. 4f), although similar patterns were not observed in
344 cynomolgus monkeys.

345 CD8 depletion also differentially modulated the abundance of monocyte subsets in blood. One
346 day following ZIKV infection, classical monocytes expanded immediately in nondepleted
347 animals of both cohorts (Fig. 3e) excluding the mock-depleted cynomolgus macaque C84545.
348 During acute infection (3-7 dpi), the frequency of nonclassical monocytes increased
349 preferentially in CD8-depleted rhesus macaques and in nondepleted cynomolgus macaques (Fig.
350 3f). Nondepleted rhesus macaques showed an expansion of intermediate monocyte frequency at
351 3-7 dpi (Fig. 3g), although a CD8-dependent effect on intermediate monocyte frequency was not
352 evident in cynomolgus monkeys.

353 **Compensatory adaptive immune responses**
354 Adaptive immune responses to ZIKV were also differentially modulated by CD8 depletion, with
355 apparent compensatory responses in CD8-depleted macaques of both cohorts. Nondepleted
356 rhesus and cynomolgus macaques began to mount CD8 T cell responses 7-10 dpi, which were
357 characterized by proliferation (Ki67) and activation (CD69) of effector memory (EM), central
358 memory (CM), and naïve CD8 T cell subsets (Figs. 4a-c & Supplementary Figs 5a-e). These
359 responses were antigen-specific and functional, given that CD8 T cells stimulated with ZIKV
360 peptides produced IFNγ and contained perforin by intracellular cytokine staining (ICS) (Fig. 4e).
361 Intriguingly, the CD8-depleted rhesus macaque R64357 also showed evidence of a CD8 T cell
362 response at 21 dpi (Figs. 4c & 4e), concomitant with the recovery of CD8+ lymphocytes in this
363 animal (Supplementary Fig. 1a). Although tested, antigen-specific T cell responses were not
364 detected by ICS in cynomolgus macaques.

365 The absence of CD8 T cells in depleted rhesus and cynomolgus macaques appeared to promote
366 the reciprocal activation and expansion of CD4 T cell subsets (Figs. 4a-b, 4d and Supplementary
367 Figs. 5f-j), mirroring the kinetics of CD8 T cell activation in nondepleted animals. CD8-depleted
368 rhesus macaques began to induce CD4 T cell responses consistent with a Th1 phenotype,
369 characterized by co-positivity for IL-2 and IFNγ, but such responses were not present in
370 nondepleted animals (Fig. 4f).

371 To gauge humoral responses to ZIKV, we conducted plaque reduction neutralization tests
372 (PRNTs) using rhesus macaque sera to quantify neutralizing antibody titers. All animals except
373 R20865 (nondepleted) showed evidence of neutralizing antibodies at 7 dpi, the earliest post-
374 infection timepoint tested (Fig. 4g). While highly neutralizing titers were detected in all animals
375 at 15 dpi, antibody concentrations declined in nondepleted animals, but not in CD8-depleted
376 animals, beyond this timepoint. Strikingly, depleted rhesus macaques retained highly
377 neutralizing antibody titers until necropsy, a finding consistent with elevated B cell activation
378 (Fig. 4h) and proliferation (Fig. 4i) in these animals.

379 **Enhanced tissue dissemination and neuropathology**
380 Given the persistence of high neutralizing antibody titers in CD8-depleted rhesus macaques, we
381 suspected that virus might be lingering in the peripheral tissues of these animals. The duration of
382 infection before necropsy differed among the rhesus (30 dpi) and cynomolgus (14 dpi) macaque
383 cohorts to identify patterns of viral dissemination and clearance over time. Informed by previous
384 reports of ZIKV tropism in macaques (Coffey et al., 2017; Hirsch et al., 2017; Osuna et al.,
385 2016b), we searched for viral RNA in lymphoid, neural, gastrointestinal (GI), and reproductive

386 tissues, as well as in semen and cerebrospinal fluid (CSF) to evaluate viral distribution in these
387 sites.

388 Relative to nondepleted animals, CD8-depleted cynomolgus macaques had markedly higher
389 levels of ZIKV RNA in the inguinal, mesenteric, and colonic lymph nodes, as well as in the
390 spleen and jejunum (Figs. 5a and 5c). All cynomolgus monkeys except C91638 (nondepleted)
391 harbored virus in the rectum without an obvious difference among treatment groups. Notably, the
392 trend of higher viral burdens in the lymphatic tissues of CD8-depleted animals was consistent in
393 rhesus macaques (Fig. 5f). CD8 depletion also appeared to promote ZIKV dissemination in the
394 semen, with both CD8-depleted cynomolgus macaques presenting semen viral loads and no viral
395 RNA detected in nondepleted animals of the same cohort (Fig. 5d). Intriguingly, the nondepleted
396 macaque C84545 (mock-depleted) showed the highest level of viral RNA in the prostate and was
397 the only animal to present virus in the testes (Fig. 5c), yet no ZIKV was detected in the semen of
398 this animal (Fig. 5d). These findings too were consistent in rhesus macaques, with virus detected
399 in the semen (Fig. 5g) and seminal vesicle (Fig. 5f) of a CD8-depleted animal and only a
400 miniscule quantity of viral RNA detected in the semen of a nondepleted animal (Fig. 5g).

401 ZIKV RNA was detected in the brainstem and subcortical white matter of C84545 (mock-
402 depleted) (Fig. 5b), and this animal also presented a high magnitude viral load in the CSF early
403 in infection, which persisted until necropsy (Fig. 5e). Exclusive of C84545 (mock-depleted),
404 CD8-depleted cynomolgus and rhesus macaques manifested CSF viral loads at least an order of
405 magnitude greater than nondepleted animals (Figs. 5e and 5h). Although ZIKV was not detected
406 in the central nervous system (CNS) of any rhesus macaque, R25671 (CD8-depleted) and
407 R64357 (CD8-depleted) manifested neural lesions at necropsy that were not present in
408 nondepleted animals. Most strikingly, the brainstem of R25671 showed an area of severe
409 multifocal to coalescing encephalomalacia which showed evidence of Wallerian degeneration,
410 characterized by vacuolation, swollen axons, and infiltration by lymphocytes and phagocytic
411 gitter cells (Fig. 5i). Gitter cells are occasionally found within dilated myelin sheaths. Scant
412 brown granular pigment (presumed hemosiderin) and a proliferative cerebral vessel adjacent to
413 the malacia may indicate that the malacia is the result of a vascular event (thromboembolism,
414 infarct, ischemia, etc.). Additionally, lymphocytic infiltrate was present in the meninges
415 surrounding the lumbar spinal cord (Fig. 5i). No gross abnormalities were noted in R64357,
416 although the sciatic nerve exhibited mild lymphocytic perivasculitis. The sciatic nerve is a
417 known site of ZIKV replication in mice depleted of CD8 cells (Elong Ngono et al., 2017).
418 Further, the brainstem contained a localized area of gliosis, an indicator of CNS damage
419 (Garman, 2011), and dilated myelin sheaths (Fig. 5j). A cause for these neural inflammatory
420 lesions was not apparent by histology.

421 **Discussion**

422 Owing to the importance of CD8+ T cells in the control of ZIKV in mice (Elong Ngono et al.,
423 2017; Huang et al., 2017), our aim was to explore whether these findings are consistent in
424 nonhuman primates. Despite a small sample size in two cohorts, the absence of CD8+
425 lymphocytes prompted immediately observable host responses that diverged from previously
426 consistent patterns of viremia and immunity. Contrasting similar experiments with simian
427 immunodeficiency virus (SIV) (Jin et al., 1999; Klatt et al., 2010), the absence of CD8+
428 lymphocytes did not overtly affect the control of serum viremia. However, the delay of serum
429 viremia in CD8-depleted macaques stood in patent contrast to patterns of acute ZIKV infection

430 observed by our own group (Supplementary Fig. 2a) and others (Dudley et al., 2016). Although a
431 mechanism underlying the delayed serum viremia remains obscure, it is possible that a lack of
432 NK cell stimulation in CD8-depleted animals may be misfiring viral replication in what would
433 otherwise be readily permissive monocytes. Indeed, monocytes engage in intercellular crosstalk
434 with NK cells (Dalbeth et al., 2004; Michel et al., 2012), and IFNγ is shown to support ZIKV
435 replication (Chaudhary et al., 2017). NK cell-derived IFNγ may activate ZIKV infected myeloid
436 cells in nondepleted animals, promoting an inflammatory milieu that favors early viral
437 replication. Alternatively, NK cells are shown to be minor reservoirs of ZIKV RNA in infected
438 humans (Michlmayr et al., 2017) and pigtail macaques (O'Connor et al., 2018), so the absence of
439 this potential target cell may contribute to the delayed serum viremia in CD8-depleted animals.
440 Additional co-culture assays may elucidate intercellular dynamics important for maintaining
441 patterns of innate immune regulation.

442 CD8 depletion also impacted the mobilization of leukocyte populations acutely following
443 infection, contrasting patterns reliably observed by our own group (Figs S2c-e) and others
444 (Osuna et al., 2016b). Macaques depleted of CD8 T cells and NK cells show little fluctuation in
445 the biomarker of inflammation NLR, indicating altered innate immune responses immediately
446 following infection. In line with these observations, mice lacking NK cells exhibit altered
447 neutrophil recruitment in a variety of infectious and noninfectious conditions (Costantini and
448 Cassatella, 2011). Neutrophil effector functions are modulated by NK cell-derived cytokines
449 (Costantini and Cassatella, 2011), a signaling axis which might have been disrupted by the
450 depletion of NK cells in macaques.

451 Confirming miscommunication within the innate immune system of CD8-depleted macaques,
452 these animals presented largely muted transcriptional activity in key virus response pathways
453 during acute infection. In nondepleted macaques, antiviral gene expression was driven
454 principally by circulating monocytes, which stood in sharp contrast to the transcriptional void
455 evident in CD8-depleted animals. Importantly, this signaling pattern was replicated in a co-
456 culture model *ex vivo*. Intercellular crosstalk between monocytes and NK cells affects
457 transcriptional responses to ZIKV infection (Lum et al., 2018), so the absence of NK cells in
458 CD8-depleted macaques might have permitted the infection to evade transcriptional induction in
459 monocytes, complementing the delayed viremia in these animals.

460 Consistent with a model of monocyte-dependent outcomes in acute ZIKV infection, CD8-
461 depleted and nondepleted macaques also differed in the magnitude and phenotype of their
462 monocyte responses during acute infection. Intermediate and nonclassical monocytes showed the
463 greatest degree of activation, agreeing with recent findings that these subsets are primary targets
464 of ZIKV in the blood (Foo et al., 2017; Jurado and Iwasaki, 2017; Michlmayr et al., 2017). CD8
465 depletion also impacted the activation of monocytes temporally, further underscoring
466 dysregulated innate responses in depleted animals. CD169 (siglec-1) is a sialic acid-binding
467 lectin previously found to be upregulated in acute ZIKV infection in rhesus macaques (Hirsch et
468 al., 2018; Hirsch et al., 2017). CD169 has important roles in virus capture by myeloid cells
469 (Sewald et al., 2015) and in the mounting of CD8 T cell responses in viral infection (van Dinther
470 et al., 2018), so the robust induction of CD169 in nondepleted animals might have promoted
471 sufficient CD8 T cell responses. CD8 depletion also affected monocyte frequency, possibly
472 contributing to differential transcriptional responses. The transient increase in classical
473 monocytes of both cohorts may be analogous to the monocytosis that accompanies acute ZIKV
474 replication in human patients (Michlmayr et al., 2017). The increase in CD16+ nonclassical

475 monocytes in CD8-depleted rhesus macaques is an outcome also observed in ZIKV infection of
476 human blood (Foo et al., 2017), and the expansion of intermediate monocytes in nondepleted
477 animals resembles ZIKV infection in Nicaraguan patients (Michlmayr et al., 2017). Although
478 minor species differences were evident in the immunophenotyping of rhesus and cynomolgus
479 monocytes, our data support a CD8+ lymphocyte-dependent effect in these transitions, possibly
480 accounting for divergent transcriptional responses in blood.

481 In addition to modulating innate immune responses, the depletion of CD8+ lymphocytes also
482 promoted compensatory adaptive responses to ZIKV in both cohorts. Nondepleted animals and
483 even the CD8-recovering rhesus macaque R64357 mounted robust CD8 T cell responses,
484 affirming the importance of CD8+ lymphocytes in acute infection. There is precedence for CD8
485 T cell responses to ZIKV in mice (Elong Ngono et al., 2017; Huang et al., 2017; Pardy et al.,
486 2017) and humans (Grifoni et al., 2018; Grifoni et al., 2017), which appears to be consistent in
487 nonhuman primates. Meanwhile, the presence of Th1 responses and prolonged humoral
488 responses in CD8-depleted animals possibly compensate for the absence of CD8 surveillance.
489 Such adaptive responses are reported in mice, as Th1 polarization (Pardy et al., 2017), and CD4-
490 driven humoral responses (Lucas et al., 2018) are important for controlling infection. Our data
491 support the importance of these adaptive responses in nonhuman primates, especially when the
492 CD8 arm of adaptive immunity is compromised.

493 The persistence of high neutralizing antibody titers until necropsy in CD8-depleted rhesus
494 macaques also suggested that there might be virus lingering in the peripheral tissues of these
495 animals. Indeed, ZIKV RNA was generally more abundant in the lymphatic tissues, semen and
496 CSF of CD8-depleted rhesus and cynomolgus macaques relative to nondepleted animals,
497 implying the importance of CD8+ lymphocytes in limiting ZIKV dissemination and/or
498 persistence in tissues. Lymphatic tissue viral loads were also consistently higher in cynomolgus
499 compared to rhesus macaques, possibly reflecting the abbreviated time of infection before
500 necropsy. Despite the detection of viral RNA in semen, ZIKV was scarce in reproductive tissues,
501 in line with an absence of gross pathological lesions including atrophy of the testes. Although
502 testicular atrophy is reported is murine models of ZIKV (Uraki et al., 2017), such manifestations
503 have not been observed in macaques or in clinical cases (Matusali et al., 2018). In rhesus
504 monkeys, it is possible that viral RNA in neural and reproductive tissues might have been only
505 transiently present due to viral clearance given the 30-day infection period of these animals.
506 Previous reports in rhesus (Aid et al., 2017) and pigtail (O'Connor et al., 2018) monkeys have
507 also shown that ZIKV persists in lymphatic tissues well beyond the clearance of virus from the
508 serum. It remains unclear whether the ZIKV present in lymph nodes is replication competent, but
509 our data are nonetheless consistent with a model where the absence of CD8+ lymphocytes
510 permits the dispersal of ZIKV.

511 CD8-depleted rhesus macaques also presented gross neural lesions at necropsy not seen in
512 nondepleted animals. The most severe lesion occurred in the brainstem of a depleted animal that
513 never recovered CD8+ lymphocytes, and similar manifestations of encephalomalacia and axon
514 degeneration have been reported in ZIKV infection of human fetal brain tissue (Driggers et al.,
515 2016; Petribu et al., 2018; Vesnaver et al., 2017). Perhaps complementarily, neural lesions in the
516 CD8-recovering rhesus macaque were less severe. Although it is tempting to speculate that the
517 absence of CD8+ lymphocytes in R25671 (CD8-depleted) and R64357 (CD8-depleted) allowed
518 neural dissemination of the virus and thereby promoted neuropathy, our inability to detect ZIKV
519 RNA in brain sections from these animals precludes this conclusion. Because ZIKV was cleared

520 from the CSF of rhesus monkeys within 15 dpi, it is possible that virus could have also cleared
521 from the CNS by necropsy and that these lesions were virus associated even if viral RNA was
522 not detectable late in infection. Supporting this argument, CSF viral loads appear to be associated
523 with ZIKV dissemination in neural tissue, given that the mock-depleted cynomolgus macaque
524 C84545 showed the highest and most persistent CSF viremia and was also the only animal with
525 ZIKV RNA identified in the brain. Despite the presence of CD8+ lymphocytes in C84545, this
526 animal was the sole example of neural dissemination and occasionally produced responses more
527 similar to CD8-depleted animals in key immune measures including NLR and classical
528 monocyte frequency, underscoring the importance of innate immunity in limiting viral
529 dissemination. Although it remains possible that off-target antibody effects produced
530 immunological nuances in C84545, this animal ultimately aligned more closely with nondepleted
531 animals in terms of serum viremia, antiviral gene induction, and adaptive immune activation,
532 affirming the importance of CD8+ lymphocytes in maintaining immune regulation during acute
533 ZIKV infection. The general absence of immune surveillance and IFN signaling in CD8-depleted
534 animals might have permitted initial infection of neural tissues, which might have been transient
535 due to the eventual priming of compensatory adaptive responses. Additionally, ZIKV localizes as
536 discrete foci in macaque tissues (Hirsch et al., 2018), complicating the detection of sparse viral
537 lesions within organs. It is worth noting that CNS localization of ZIKV has been observed as
538 early as 5 dpi in acutely infected macaques (Osuna et al., 2016b), and a separate study in rhesus
539 monkeys failed to identify ZIKV RNA in the CNS at 14 dpi, despite diffuse patterns of viral
540 dissemination (Coffey et al., 2017). These findings, together with our own, establish precedence
541 for early CNS dissemination of ZIKV in nonhuman primates, which may be cleared later in
542 infection.

543 In summary, the present study illustrates a pliable dynamic between ZIKV and its hosts. CD8
544 depletion appears to alter innate immune activation and antiviral signaling and also modulate
545 viral kinetics without overtly affecting serum viremia. Together with apparently compensatory
546 adaptive responses and the presence of enhanced viral tissue distribution, these findings suggest
547 that CD8 T cells provide default adaptive immune responses to ZIKV, a conclusion with
548 important consequences for immune-based interventions such as vaccine development.

549 **Acknowledgements**
550 This work was supported by a pilot award to N.J.M. from the TNPRC base grant (National
551 Institutes of Health P51OD011104). The funders had no role in study design and interpretation.

552 **Author contributions**
553 BS, AP, and NM planned the studies. BS, MF, ES, MW, KH, DS, RB, MG, LDM, and VD
554 conducted the experiments. DW and MB provided reagents. BS, MF, MW, RB, AP, and NM
555 interpreted the studies. BS and NM wrote the first draft. AP and NM obtained funding. All
556 authors reviewed, edited, and approved the paper.

557 **Conflict of Interest**
558 The authors declare no conflicts of interest.

559 **Contribution to the Field**
560 A number of reports have indicated an important role for CD8 T cells in the control of ZIKV
561 replication in mice, but these models are limited in that the mice need to be

562 immunocompromised for efficient viral infection. Using two established nonhuman primate
563 models of ZIKV infection, we found that CD8+ lymphocytes are critical in orchestrating the
564 earliest immune events during viral infection. The absence of CD8 cells enhanced viral
565 dissemination into multiple tissues and prompted immediately observable host responses that
566 diverged from previously consistent patterns of viremia and immunity. Importantly, the
567 implications of these data may reach beyond ZIKV and are likely instructive to how CD8 cells
568 interact with other immune cells to coordinate the control of viral infections generally.

569 **Materials & Correspondence**

570 Material requests and correspondence should be addressed to N.J.M. (nmaness@tulane.edu).

571 **References**

572 Aid, M., Abbink, P., Larocca, R.A., Boyd, M., Nityanandam, R., Nanayakkara, O., Martinot, A.J., Moseley,
573 E.T., Blass, E., Borducchi, E.N*., et al.* (2017). Zika Virus Persistence in the Central Nervous System and
574 Lymph Nodes of Rhesus Monkeys. Cell *169*, 610-620.e614.
575 Amir, e.-A., Davis, K.L., Tadmor, M.D., Simonds, E.F., Levine, J.H., Bendall, S.C., Shenfeld, D.K.,
576 Krishnaswamy, S., Nolan, G.P., and Pe'er, D. (2013). viSNE enables visualization of high dimensional
577 single-cell data and reveals phenotypic heterogeneity of leukemia. Nat Biotechnol *31*, 545-552.
578 Biesen, R., Demir, C., Barkhudarova, F., Grün, J.R., Steinbrich-Zöllner, M., Backhaus, M., Häupl, T.,
579 Rudwaleit, M., Riemekasten, G., Radbruch, A*., et al.* (2008). Sialic acid-binding Ig-like lectin 1 expression
580 in inflammatory and resident monocytes is a potential biomarker for monitoring disease activity and
581 success of therapy in systemic lupus erythematosus. Arthritis Rheum *58*, 1136-1145.
582 Bonaldo, M.C., Ribeiro, I.P., Lima, N.S., Dos Santos, A.A., Menezes, L.S., da Cruz, S.O., de Mello, I.S.,
583 Furtado, N.D., de Moura, E.E., Damasceno, L*., et al.* (2016). Isolation of Infective Zika Virus from Urine
584 and Saliva of Patients in Brazil. PLoS Negl Trop Dis *10*, e0004816.
585 Bryan, M.A., Giordano, D., Draves, K.E., Green, R., Gale, M., and Clark, E.A. (2018). Splenic macrophages
586 are required for protective innate immunity against West Nile virus. PLoS One *13*, e0191690.
587 Chaudhary, V., Yuen, K.S., Chan, J.F., Chan, C.P., Wang, P.H., Cai, J.P., Zhang, S., Liang, M., Kok, K.H.,
588 Yuen, K.Y*., et al.* (2017). Selective Activation of Type II Interferon Signaling by Zika Virus NS5 Protein. J
589 Virol *91*.
590 Coffey, L.L., Pesavento, P.A., Keesler, R.I., Singapuri, A., Watanabe, J., Watanabe, R., Yee, J., Bliss-
591 Moreau, E., Cruzen, C., Christe, K.L*., et al.* (2017). Zika Virus Tissue and Blood Compartmentalization in
592 Acute Infection of Rhesus Macaques. PLoS One *12*, e0171148.
593 Costantini, C., and Cassatella, M.A. (2011). The defensive alliance between neutrophils and NK cells as a
594 novel arm of innate immunity. J Leukoc Biol *89*, 221-233.
595 Dalbeth, N., Gundle, R., Davies, R.J., Lee, Y.C., McMichael, A.J., and Callan, M.F. (2004). CD56bright NK
596 cells are enriched at inflammatory sites and can engage with monocytes in a reciprocal program of
597 activation. J Immunol *173*, 6418-6426.
598 Dick, G.W., Kitchen, S.F., and Haddow, A.J. (1952). Zika virus. I. Isolations and serological specificity.
599 Trans R Soc Trop Med Hyg *46*, 509-520.
600 Driggers, R.W., Ho, C.Y., Korhonen, E.M., Kuivanen, S., Jaaskelainen, A.J., Smura, T., Rosenberg, A., Hill,
601 D.A., DeBiasi, R.L., Vezina, G*., et al.* (2016). Zika Virus Infection with Prolonged Maternal Viremia and
602 Fetal Brain Abnormalities. N Engl J Med *374*, 2142-2151.
603 Dudley, D.M., Aliota, M.T., Mohr, E.L., Weiler, A.M., Lehrer-Brey, G., Weisgrau, K.L., Mohns, M.S.,
604 Breitbach, M.E., Rasheed, M.N., Newman, C.M*., et al.* (2016). A rhesus macaque model of Asian-lineage
605 Zika virus infection. Nat Commun *7*, 12204.

606 Dudley, D.M., Van Rompay, K.K., Coffey, L.L., Ardeshir, A., Keesler, R.I., Bliss-Moreau, E., Grigsby, P.L.,
607 Steinbach, R.J., Hirsch, A.J., MacAllister, R.P.*, et al.* (2018). Miscarriage and stillbirth following maternal
608 Zika virus infection in nonhuman primates. Nature medicine *24*, 1104-1107.
609 Elong Ngono, A., Vizcarra, E.A., Tang, W.W., Sheets, N., Joo, Y., Kim, K., Gorman, M.J., Diamond, M.S.,
610 and Shresta, S. (2017). Mapping and Role of the CD8(+) T Cell Response During Primary Zika Virus
611 Infection in Mice. Cell Host Microbe *21*, 35-46.
612 Faria, S.S., Fernandes, P.C., Silva, M.J., Lima, V.C., Fontes, W., Freitas-Junior, R., Eterovic, A.K., and
613 Forget, P. (2016). The neutrophil-to-lymphocyte ratio: a narrative review. Ecancermedicalscience *10*,
614 702.
615 Foo, S.S., Chen, W., Chan, Y., Bowman, J.W., Chang, L.C., Choi, Y., Yoo, J.S., Ge, J., Cheng, G., Bonnin, A.*,*
616 *et al.* (2017). Asian Zika virus strains target CD14+ blood monocytes and induce M2-skewed
617 immunosuppression during pregnancy. Nat Microbiol *2*, 1558-1570.
618 Garman, R.H. (2011). Histology of the central nervous system. Toxicol Pathol *39*, 22-35.
619 Grant, A., Ponia, S.S., Tripathi, S., Balasubramaniam, V., Miorin, L., Sourisseau, M., Schwarz, M.C.,
620 Sanchez-Seco, M.P., Evans, M.J., Best, S.M.*, et al.* (2016). Zika Virus Targets Human STAT2 to Inhibit Type
621 I Interferon Signaling. Cell host & microbe *19*, 882-890.
622 Grifoni, A., Costa-Ramos, P., Pham, J., Tian, Y., Rosales, S.L., Seumois, G., Sidney, J., de Silva, A.D.,
623 Premkumar, L., Collins, M.H.*, et al.* (2018). Cutting Edge: Transcriptional Profiling Reveals Multifunctional
624 and Cytotoxic Antiviral Responses of Zika Virus-Specific CD8. J Immunol *201*, 3487-3491.
625 Grifoni, A., Pham, J., Sidney, J., O'Rourke, P.H., Paul, S., Peters, B., Martini, S.R., de Silva, A.D., Ricciardi,
626 M.J., Magnani, D.M.*, et al.* (2017). Prior Dengue virus exposure shapes T cell immunity to Zika virus in
627 humans. J Virol.
628 Hirsch, A.J., Roberts, V.H.J., Grigsby, P.L., Haese, N., Schabel, M.C., Wang, X., Lo, J.O., Liu, Z., Kroenke,
629 C.D., Smith, J.L.*, et al.* (2018). Zika virus infection in pregnant rhesus macaques causes placental
630 dysfunction and immunopathology. Nat Commun *9*, 263.
631 Hirsch, A.J., Smith, J.L., Haese, N.N., Broeckel, R.M., Parkins, C.J., Kreklywich, C., DeFilippis, V.R., Denton,
632 M., Smith, P.P., Messer, W.B.*, et al.* (2017). Zika Virus infection of rhesus macaques leads to viral
633 persistence in multiple tissues. PLoS pathogens *13*, e1006219.
634 Huang, H., Li, S., Zhang, Y., Han, X., Jia, B., Liu, H., Liu, D., Tan, S., Wang, Q., Bi, Y.*, et al.* (2017). CD8+ T
635 Cell Immune Response in Immunocompetent Mice during Zika Virus Infection. J Virol *91*.
636 Jin, X., Bauer, D.E., Tuttleton, S.E., Lewin, S., Gettie, A., Blanchard, J., Irwin, C.E., Safrit, J.T., Mittler, J.,
637 Weinberger, L.*, et al.* (1999). Dramatic rise in plasma viremia after CD8(+) T cell depletion in simian
638 immunodeficiency virus-infected macaques. J Exp Med *189*, 991-998.
639 Jurado, K.A., and Iwasaki, A. (2017). Zika virus targets blood monocytes. Nat Microbiol *2*, 1460-1461.
640 Jurado, K.A., Yockey, L.J., Wong, P.W., Lee, S., Huttner, A.J., and Iwasaki, A. (2018). Antiviral CD8 T cells
641 induce Zika-virus-associated paralysis in mice. Nat Microbiol *3*, 141-147.
642 Klatt, N.R., Shudo, E., Ortiz, A.M., Engram, J.C., Paiardini, M., Lawson, B., Miller, M.D., Else, J., Pandrea,
643 I., Estes, J.D.*, et al.* (2010). CD8+ lymphocytes control viral replication in SIVmac239-infected rhesus
644 macaques without decreasing the lifespan of productively infected cells. PLoS Pathog *6*, e1000747.
645 Koide, F., Goebel, S., Snyder, B., Walters, K.B., Gast, A., Hagelin, K., Kalkeri, R., and Rayner, J. (2016).
646 Development of a Zika Virus Infection Model in Cynomolgus Macaques. Front Microbiol *7*, 2028.
647 Lieberman, M.M., Nerurkar, V.R., Luo, H., Cropp, B., Carrion, R., de la Garza, M., Coller, B.A., Clements,
648 D., Ogata, S., Wong, T.*, et al.* (2009). Immunogenicity and protective efficacy of a recombinant subunit
649 West Nile virus vaccine in rhesus monkeys. Clin Vaccine Immunol *16*, 1332-1337.
650 Lucas, C.G.O., Kitoko, J.Z., Ferreira, F.M., Suzart, V.G., Papa, M.P., Coelho, S.V.A., Cavazzoni, C.B., Paula-
651 Neto, H.A., Olsen, P.C., Iwasaki, A.*, et al.* (2018). Critical role of CD4+ T cells and IFNγ signaling in
652 antibody-mediated resistance to Zika virus infection. Nat Commun *9*.

653 Lum, F.M., Lee, D., Chua, T.K., Tan, J.J.L., Lee, C.Y.P., Liu, X., Fang, Y., Lee, B., Yee, W.X., Rickett, N.Y.*, et*
654 *al.* (2018). Zika Virus Infection Preferentially Counterbalances Human Peripheral Monocyte and/or NK
655 Cell Activity. mSphere *3*.
656 Magnani, D.M., Rogers, T.F., Maness, N.J., Grubaugh, N.D., Beutler, N., Bailey, V.K., Gonzalez-Nieto, L.,
657 Gutman, M.J., Pedreno-Lopez, N., Kwal, J.M.*, et al.* (2018a). Fetal demise and failed antibody therapy
658 during Zika virus infection of pregnant macaques. Nature communications *9*, 1624.
659 Magnani, D.M., Rogers, T.F., Maness, N.J., Grubaugh, N.D., Beutler, N., Bailey, V.K., Gonzalez-Nieto, L.,
660 Gutman, M.J., Pedreño-Lopez, N., Kwal, J.M.*, et al.* (2018b). Fetal demise and failed antibody therapy
661 during Zika virus infection of pregnant macaques. Nat Commun *9*, 1624.
662 Matusali, G., Houzet, L., Satie, A.P., Mahé, D., Aubry, F., Couderc, T., Frouard, J., Bourgeau, S., Bensalah,
663 K., Lavoué, S.*, et al.* (2018). Zika virus infects human testicular tissue and germ cells. J Clin Invest *128*,
664 4697-4710.
665 Metsalu, T., and Vilo, J. (2015). ClustVis: a web tool for visualizing clustering of multivariate data using
666 Principal Component Analysis and heatmap. Nucleic Acids Res *43*, W566-570.
667 Michel, T., Hentges, F., and Zimmer, J. (2012). Consequences of the crosstalk between
668 monocytes/macrophages and natural killer cells. Front Immunol *3*, 403.
669 Michlmayr, D., Andrade, P., Gonzalez, K., Balmaseda, A., and Harris, E. (2017). CD14+CD16+ monocytes
670 are the main target of Zika virus infection in peripheral blood mononuclear cells in a paediatric study in
671 Nicaragua. Nat Microbiol *2*, 1462-1470.
672 O'Connor, M.A., Tisoncik-Go, J., Lewis, T.B., Miller, C.J., Bratt, D., Moats, C.R., Edlefsen, P.T., Smedley, J.,
673 Klatt, N.R., Gale, M.*, et al.* (2018). Early cellular innate immune responses drive Zika viral persistence and
674 tissue tropism in pigtail macaques. Nat Commun *9*, 3371.
675 Osuna, C.E., Lim, S.Y., Deleage, C., Griffin, B.D., Stein, D., Schroeder, L.T., Omange, R., Best, K., Luo, M.,
676 Hraber, P.T.*, et al.* (2016a). Zika viral dynamics and shedding in rhesus and cynomolgus macaques.
677 Nature medicine *22*, 1448-1455.
678 Osuna, C.E., Lim, S.Y., Deleage, C., Griffin, B.D., Stein, D., Schroeder, L.T., Omange, R.W., Best, K., Luo,
679 M., Hraber, P.T.*, et al.* (2016b). Zika viral dynamics and shedding in rhesus and cynomolgus macaques.
680 Nat Med *22*, 1448-1455.
681 Pardy, R.D., Rajah, M.M., Condotta, S.A., Taylor, N.G., Sagan, S.M., and Richer, M.J. (2017). Analysis of
682 the T Cell Response to Zika Virus and Identification of a Novel CD8+ T Cell Epitope in Immunocompetent
683 Mice. PLoS Pathog *13*, e1006184.
684 Petribu, N.C.L., Fernandes, A.C.V., Abath, M.B., Araújo, L.C., de Queiroz, F.R.S., Araújo, J.M., de Carvalho,
685 G.B., and van der Linden, V. (2018). Common findings on head computed tomography in neonates with
686 confirmed congenital Zika syndrome. Radiol Bras *51*, 366-371.
687 Plourde, A.R., and Bloch, E.M. (2016). A Literature Review of Zika Virus. Emerg Infect Dis *22*, 1185-1192.
688 Prestwood, T.R., May, M.M., Plummer, E.M., Morar, M.M., Yauch, L.E., and Shresta, S. (2012). Trafficking
689 and replication patterns reveal splenic macrophages as major targets of dengue virus in mice. J Virol *86*,
690 12138-12147.
691 R Core Team (2018). R: A language and environment for statistical computing (Vienna, Austria: R
692 Foundation for Statistical Computing).
693 Schmitz, J.E., Simon, M.A., Kuroda, M.J., Lifton, M.A., Ollert, M.W., Vogel, C.W., Racz, P., Tenner-Racz, K.,
694 Scallon, B.J., Dalesandro, M.*, et al.* (1999). A nonhuman primate model for the selective elimination of
695 CD8+ lymphocytes using a mouse-human chimeric monoclonal antibody. Am J Pathol *154*, 1923-1932.
696 Sewald, X., Ladinsky, M.S., Uchil, P.D., Beloor, J., Pi, R., Herrmann, C., Motamedi, N., Murooka, T.T.,
697 Brehm, M.A., Greiner, D.L.*, et al.* (2015). Retroviruses use CD169-mediated trans-infection of permissive
698 lymphocytes to establish infection. Science *350*, 563-567.
699 Slon Campos, J.L., Mongkolsapaya, J., and Screaton, G.R. (2018). The immune response against
700 flaviviruses. Nat Immunol *19*, 1189-1198.

701 Swirski, F.K., Nahrendorf, M., Etzrodt, M., Wildgruber, M., Cortez-Retamozo, V., Panizzi, P., Figueiredo,
702 J.L., Kohler, R.H., Chudnovskiy, A., Waterman, P.*, et al.* (2009). Identification of splenic reservoir
703 monocytes and their deployment to inflammatory sites. Science *325*, 612-616.
704 Uraki, R., Hwang, J., Jurado, K.A., Householder, S., Yockey, L.J., Hastings, A.K., Homer, R.J., Iwasaki, A.,
705 and Fikrig, E. (2017). Zika virus causes testicular atrophy. Sci Adv *3*, e1602899.
706 van Dinther, D., Veninga, H., Iborra, S., Borg, E.G.F., Hoogterp, L., Olesek, K., Beijer, M.R., Schetters,
707 S.T.T., Kalay, H., Garcia-Vallejo, J.J.*, et al.* (2018). Functional CD169 on Macrophages Mediates
708 Interaction with Dendritic Cells for CD8. Cell Rep *22*, 1484-1495.
709 Vesnaver, T.V., Tul, N., Mehrabi, S., Parissone, F., Strafela, P., Mlakar, J., Pizem, J., Korva, M., Zupanc,
710 T.A., and Popovic, M. (2017). Zika virus associated microcephaly/micrencephaly-fetal brain imaging in
711 comparison with neuropathology. BJOG *124*, 521-525.
712 Ward, M.J., Alger, J., Berrueta, M., Bock, H., Buekens, P., Cafferata, M.L., Ciganda, A., García, J., García,
713 K., Lopez, W.*, et al.* (2018). Zika Virus and the World Health Organization Criteria for Determining Recent
714 Infection Using Plaque Reduction Neutralization Testing. Am J Trop Med Hyg *99*, 780-782.
715 York, M.R., Nagai, T., Mangini, A.J., Lemaire, R., van Seventer, J.M., and Lafyatis, R. (2007). A
716 macrophage marker, Siglec-1, is increased on circulating monocytes in patients with systemic sclerosis
717 and induced by type I interferons and toll-like receptor agonists. Arthritis Rheum *56*, 1010-1020.

718 **Figure legends**

719 **Figure 1**

720 Delayed serum viremia and altered leukocyte kinetics in CD8-depleted macaques. (**A**) Study
721 design. Two animals of each cohort were depleted of CD8+ lymphocytes, and all animals were
722 infected with a Brazilian isolate of ZIKV. Viremia was tracked over 30 days in cohort 1 and 14
723 days in cohort 2 before necropsy. Colors used in the timeline correspond to cohorts and treatment
724 conditions. C46456 (nondepleted) was splenectomized in a previous study and is indicated by an
725 asterisk (*) throughout. (**B**) Flow cytometric analysis of CD8 T cell frequencies in PBMCs over
726 time. (*Top*): cohort 1; (*Bottom*): cohort 2 (consistent throughout). (**C**) NK cell frequency, as
727 measured by flow cytometry. (**D**) Viral RNA in serum over infection (error bars, SD). (**E**) NLR,
728 derived using total neutrophil and lymphocyte counts in blood from CBC data. (**F**) Fold change
729 in NLR from 0 to 1 dpi among 4 rhesus and 4 cynomolgus macaques included in the present
730 study in addition to a previous cohort of 4 ZIKV-infected non-pregnant female rhesus macaques
731 (center line, mean; error bars, SD). (The blood of one CD8-depleted cynomolgus macaque,
732 C18942, clotted prior to complete blood count (CBC) analysis, precluding calculation of NLR
733 for this animal.) The significant ($p \leq 0.05$) difference in NLR fold change was determined using
734 a Mann-Whitney test.

735 **Figure 2**

736 Differential monocyte-driven transcriptional profiles among CD8-depleted and nondepleted
737 macaques. (**A**) Activation of downstream IFNα effector molecules in whole blood at 3 dpi
738 relative to pre-infection (cyno. = cynomolgus, consistent throughout). **(B)** Fold regulation of
739 antiviral gene expression in whole blood at 3 dpi, confirmed using a qRT-PCR array of 84 genes
740 in the rhesus macaque genome (dep. = CD8-depleted; non. = nondepleted). **(C)** PCA of antiviral
741 gene expression in whole blood at 3 dpi. **(D)** Activation of downstream IFNα effector molecules
742 in sorted CD14+ monocytes and CD14- PBMCs at 3 dpi. **(E)** qPCR confirmation of antiviral
743 gene expression in CD14+ monocytes and CD14- PBMCs at 3 dpi. Gene induction is normalized
744 to b-actin, and fold regulation is expressed relative to 0 dpi. **(F)** Antiviral gene expression in
745 CD8+ and CD8- fractions of PBMCs from a nondepleted rhesus macaque at 3 dpi. Gene

746 induction is normalized to b-actin, and fold regulation is expressed relative to 15 dpi. **(G)**
747 Antiviral gene expression in co-cultured CD14+ monocytes and autologous CD8+ cells from
748 ZIKV-naïve PBMC infected with ZIKV *ex vivo* at 1 and 3 dpi. **(H)** Comparison of antiviral gene
749 induction in cultured, ZIKV-infected MDMs (red) and the whole blood of nondepleted rhesus
750 (blue) and cynomolgus (green) macaques at 3 dpi. Genes included in the qPCR array relate to
751 toll-like receptor (TLR), nod-like receptor (NLR) or type-I interferon (IFN-I) signaling (resp. =
752 responsive).

753 **Figure 3**
754 Altered monocyte activation and frequency in CD8-depleted macaques. (**A-B**) viSNE analyses of
755 monocyte activation in rhesus (A) and cynomolgus (B) macaques, as measured by CD169 mean
756 fluorescence intensity (MFI). Dot plots are concatenated for animals within each treatment
757 condition. The viSNE clustering profile of monocyte subsets (*left*) correspond to cell populations
758 in the CD169 MFI heatmaps in nondepleted and CD8-depleted animals over time (*right*). **(C)**
759 summaries of CD169 expression in total monocytes. **(D)** Induction of genes related to myeloid
760 cell activation at 3 dpi relative to pre-infection. (**E-G**) Frequencies of classical (E), nonclassical
761 (F), and intermediate (G) monocyte subsets in rhesus and cynomolgus macaques over time.

762 **Figure 4**
763 Compensatory adaptive immune responses in CD8-depleted macaques. (**A-B**) viSNE analyses of
764 T cell activation in rhesus (A) and cynomolgus (B) macaques, as measured by CD69 expression.
765 Dot plots are concatenated for animals within each treatment condition. The viSNE clustering
766 profiles of CD4 and CD8 T cell subsets (*left*) correspond to cell populations in the CD69
767 heatmaps in nondepleted and CD8-depleted animals at 1 & 10 dpi (*right*). (**C**) Proliferation of
768 EM CD8 T cells in rhesus and cynomolgus macaques over time. CD8-depleted macaques are
769 excluded owing to the absence of CD8+ lymphocytes in these animals exclusive of R64357 at
770 later timepoints. (**D**) Proliferation of EM CD4 T cells in rhesus and cynomolgus macaques over
771 time. **(E)** CD8 T cell responses in rhesus macaques, assessed by ICS of PBMCs stimulated with
772 viral peptides derived from the indicated ZIKV proteins (C = capsid; M = membrane; E =
773 envelope; NS1 = nonstructural protein 1, consistent throughout). CD8 T cell responses were
774 identified by co-positivity for perforin and IFNγ. (**F**) Th1 responses, determined by ICS for IL-2
775 and IFNγ co-positivity. (*Inset*): representative antigen-specific cytometry plots for R64357
776 (CD8-depleted) at 30 dpi. (**G**) Serum neutralizing antibody titers in rhesus macaques, represented
777 as PRNT90. **(H)** Activation of B cells in rhesus macaques over time. **(I)** Proliferation of B cells
778 in rhesus and cynomolgus macaques over time.

779 **Figure 5**
780 Enhanced tissue dissemination and neuropathology in CD8-depleted macaques. (**A-E**) Viral
781 dissemination in cynomolgus macaques, including lymphatic (A), neural (B) and reproductive
782 (C) tissues, as well as semen (D) and CSF (E) (center line, mean; error bars, SD of two replicates
783 per sample, LN = lymph node; sub. wt. matter = subcortical white matter, consistent throughout).
784 **(F-H)** Viral dissemination in rhesus macaques, including lymphatic, neural, and reproductive
785 tissues (F), as well as semen (G) and CSF (H). (**I**) R25671 (CD8-depleted) brainstem (top) and
786 lumbar spinal cord (bottom). *Top*: There is an area of encephalomalacia (dotted region, left)
787 adjacent to a vessel that exhibits medial thickening (arrow, left). The area of malacia is
788 characterized by dilated myelin sheaths with swollen axons (arrow, right) or gitter cell
789 infiltration (asterisks, right). H&E, Bar = 100 um. *Bottom*: The meninges surrounding the lumbar
790 spinal cord are multifocally infiltrated by aggregates of lymphocytes (arrows). H&E, Bar = 1 mm

791 (left) and 100 um (right). (**J**) R64357 (CD8-depleted) sciatic nerve (top) and brainstem lesions
792 (bottom). *Top*: Small vessels within the sciatic nerve are surrounded by low numbers of
793 lymphocytes (arrows). *Bottom*: A focal glial nodule is present within the gray matter of the
794 brainstem (dotted region, left) with dilation of adjacent myelin sheaths and spheroid formation
795 (arrowhead, right). H&E, Bar = 100 um.

796 **Figure S1**
797 MT807R1 depletes CD8+ lymphocytes with variable recovery. **(A)** Absolute CD8 T cell counts
798 in blood, as determined by complete blood count (CBC). **(B-C)** Absolute counts of CD4+/CD8+
799 double-positive T cells (B) and (C) CD4 T cells prior to infection, determined by CBC.

800 **Figure S2**
801 Comparison of virus and immune cell dynamics to a previous female cohort. Data from a
802 previous cohort of ZIKV-infected non-pregnant female rhesus macaques is shown in gray, and
803 data from rhesus macaques of the present study is overlaid. (**A**) Serum viral loads over the course
804 of the studies (error bars, SD). (**B**) CSF viral loads over the course of the studies. (**C-D**)
805 Frequencies of neutrophils (C) and total lymphocytes (D) in whole blood over time, determined
806 by CBC. **(E)** NLR, derived using total neutrophil and lymphocyte CBC data.

807 **Figure S3**
808 Transcriptional responses correlate with serum viremia in nondepleted macaques. **(A-B)** Pathway
809 analysis of gene expression in whole blood at 3 dpi relative to pre-infection reveals the induction
810 of genes related to leukocyte homing (A) as well as differentially activated biological functions
811 and disease-related pathways among CD8-depleted and non-depleted animals (B). **(C-D)**
812 Patterns of antiviral gene induction at 1, 3, and 15 dpi in the whole blood of nondepleted (C) and
813 CD8-depleted (D) rhesus macaques relative to pre-infection.

814 **Figure S4**
815 CD8 depletion modulates monocyte phenotype during ZIKV infection. (**A-C**) Flow cytometric
816 analysis of monocyte activation, as measured by CD169 expression in classical (A), intermediate
817 (B), and nonclassical (C) subsets in rhesus and cynomolgus macaques. (**D**) Overall monocyte
818 activation, as measured by CD69 expression. (**E-F**) Expression of CD95 in classical (E) and
819 nonclassical (F) subsets.

820 **Figure S5**
821 Reciprocal T cell responses are polyphenotypic. (**A-E**) Immunophenotyping of CD8 T cells in
822 rhesus and cynomolgus macaques, including EM CD8 activation (A), CM CD8 activation (B)
823 and proliferation (C), and naïve CD8 activation (D) and proliferation (E). **(F-J)**
824 Immunophenotyping of CD4 T cells, including EM CD4 activation (F), CM CD4 activation (G)
825 and proliferation (H), and naïve CD4 activation (I) and proliferation (J).

Fig 1: Delayed serum viremia and altered leukocyte kinetics

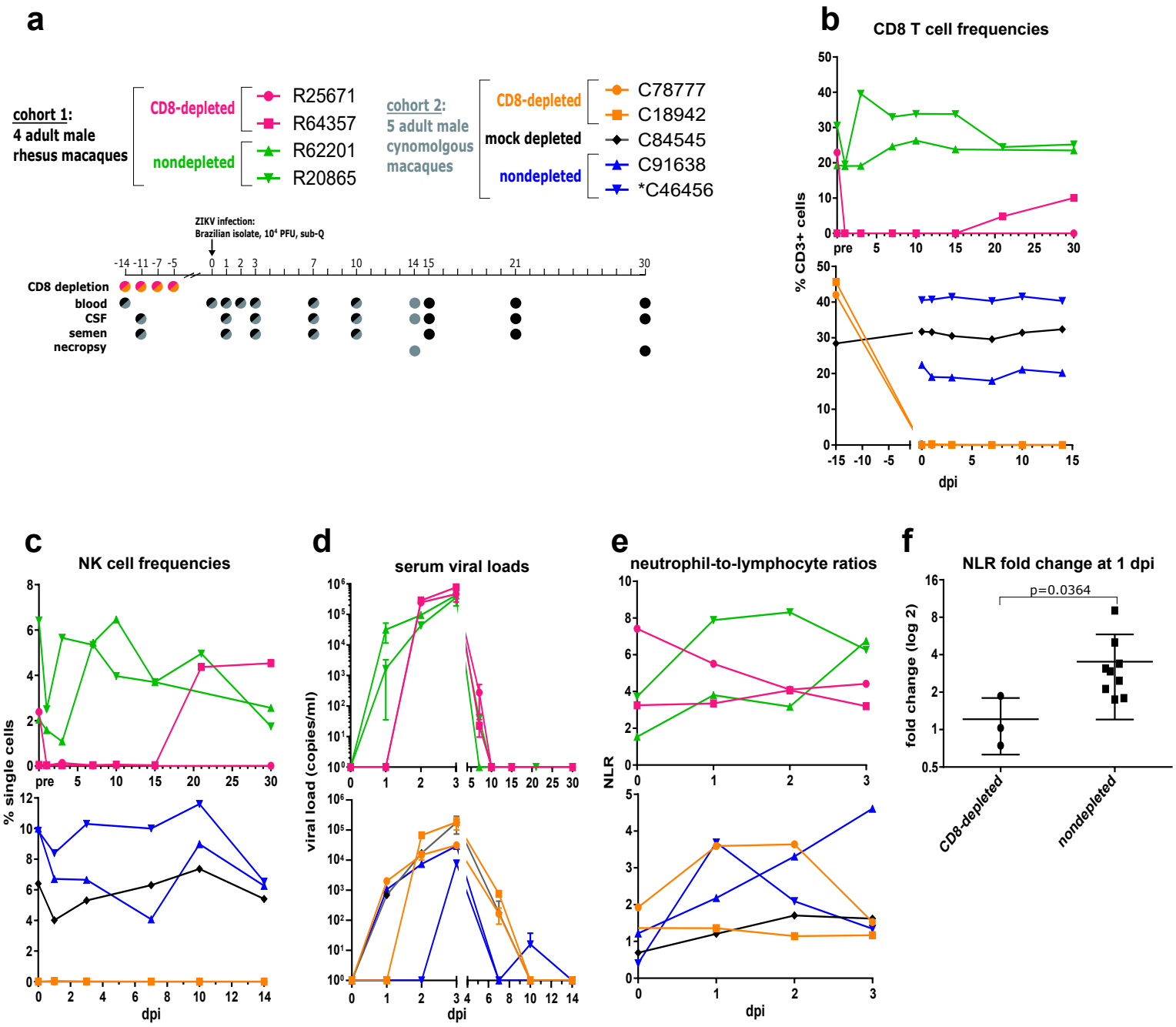

Fig 2: Differential monocyte-driven transcriptional profiles

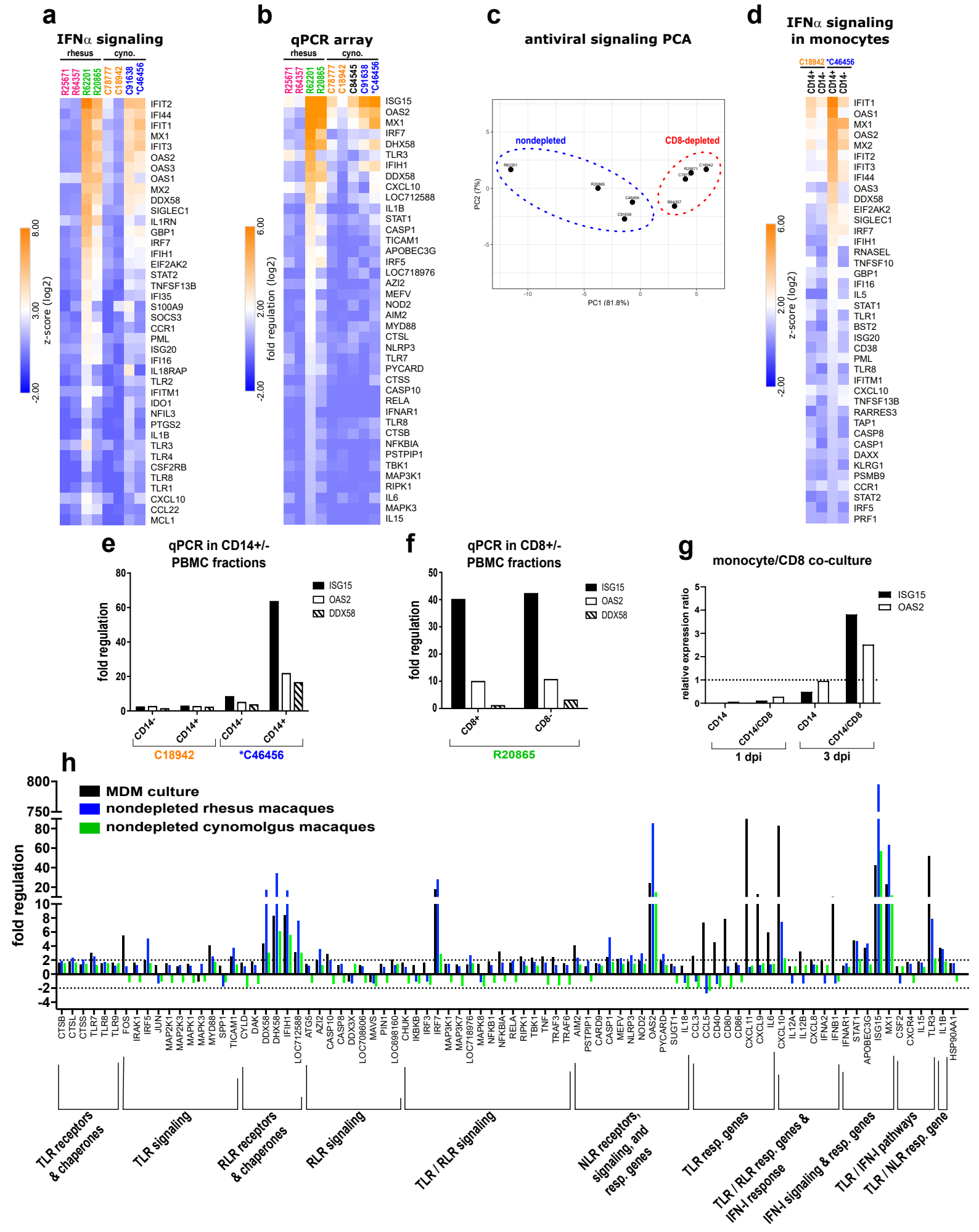

Fig 3: Altered monocyte activation and frequency

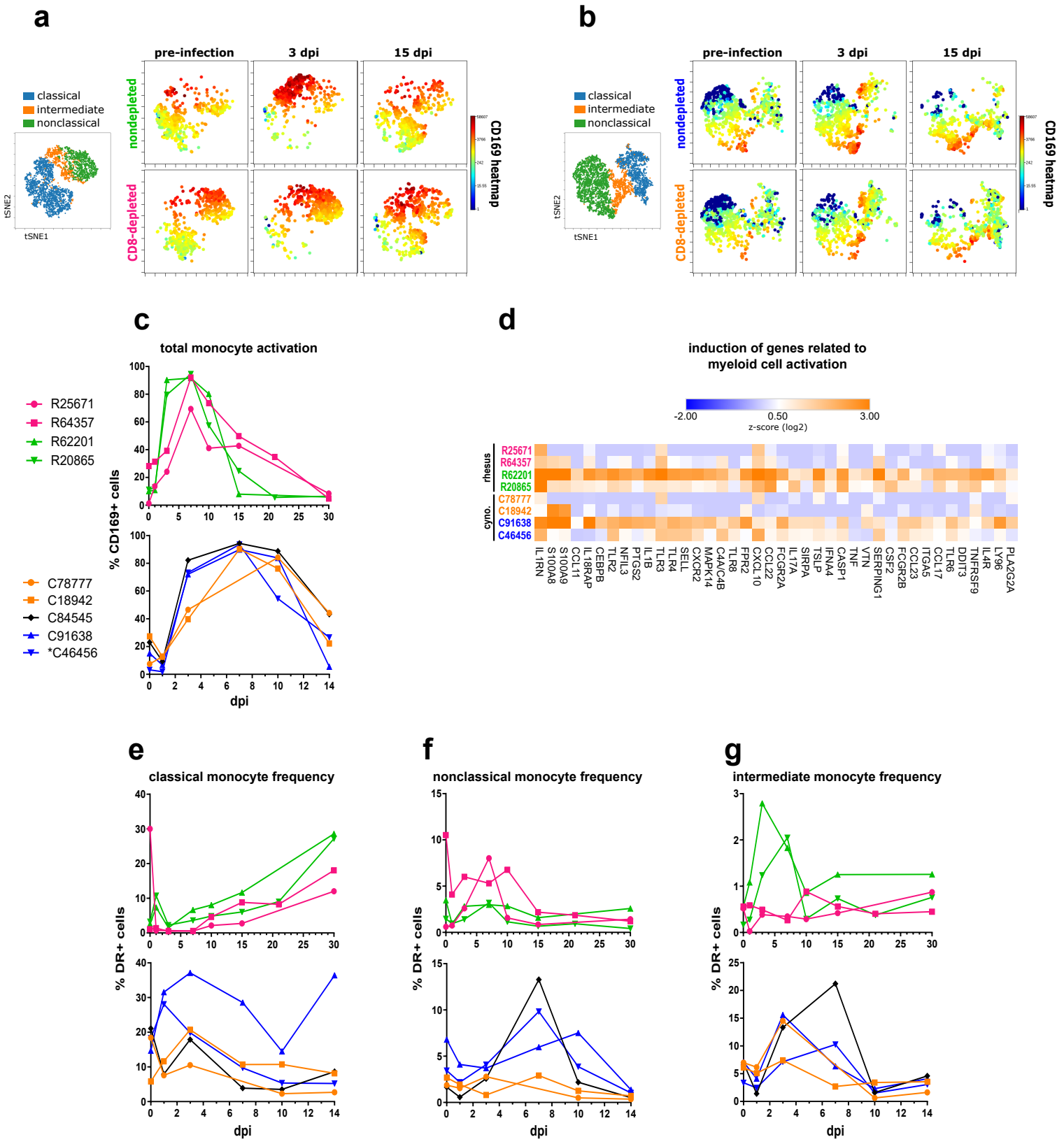

Fig 4: Compensatory CD4 and humoral responses

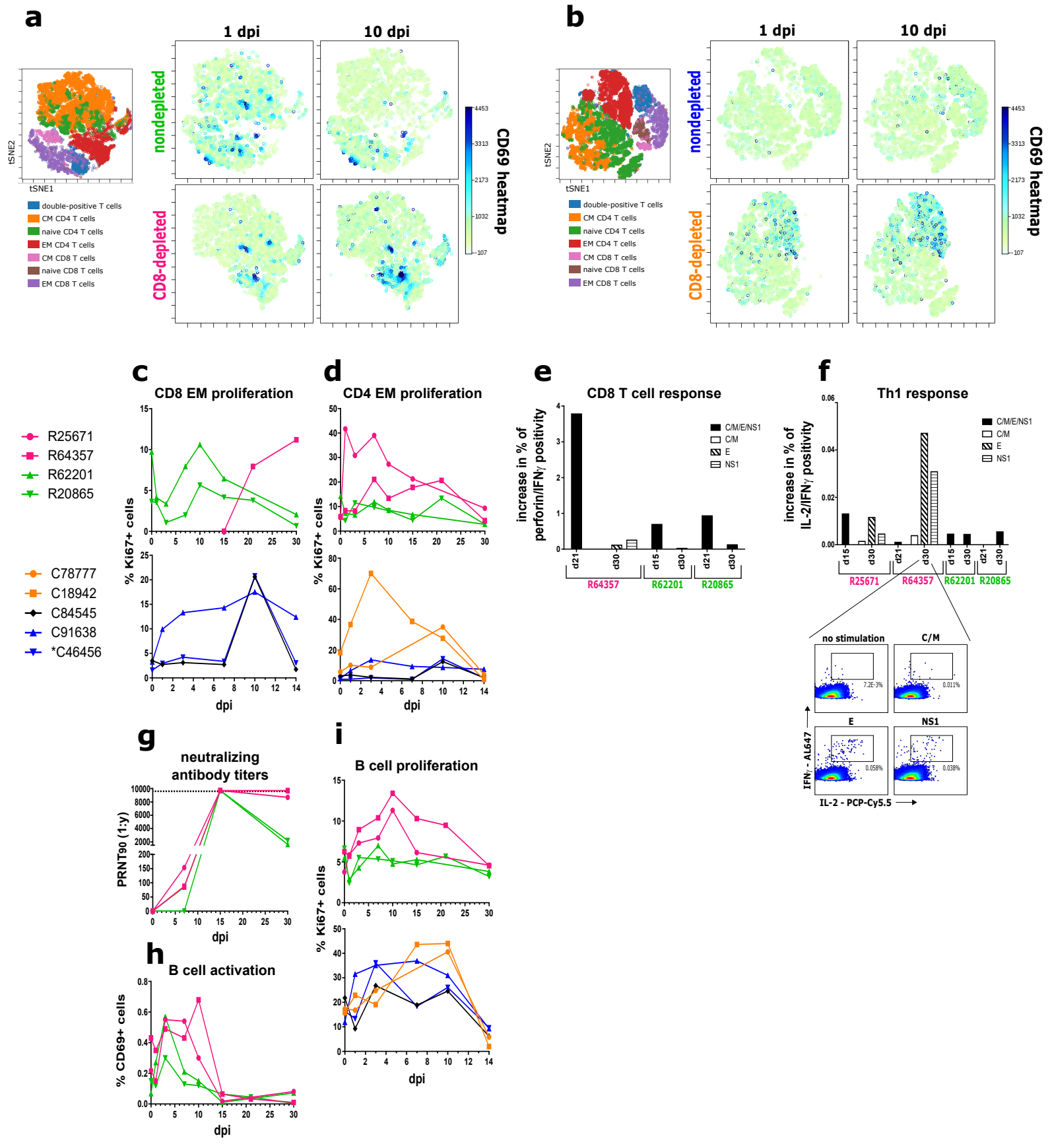
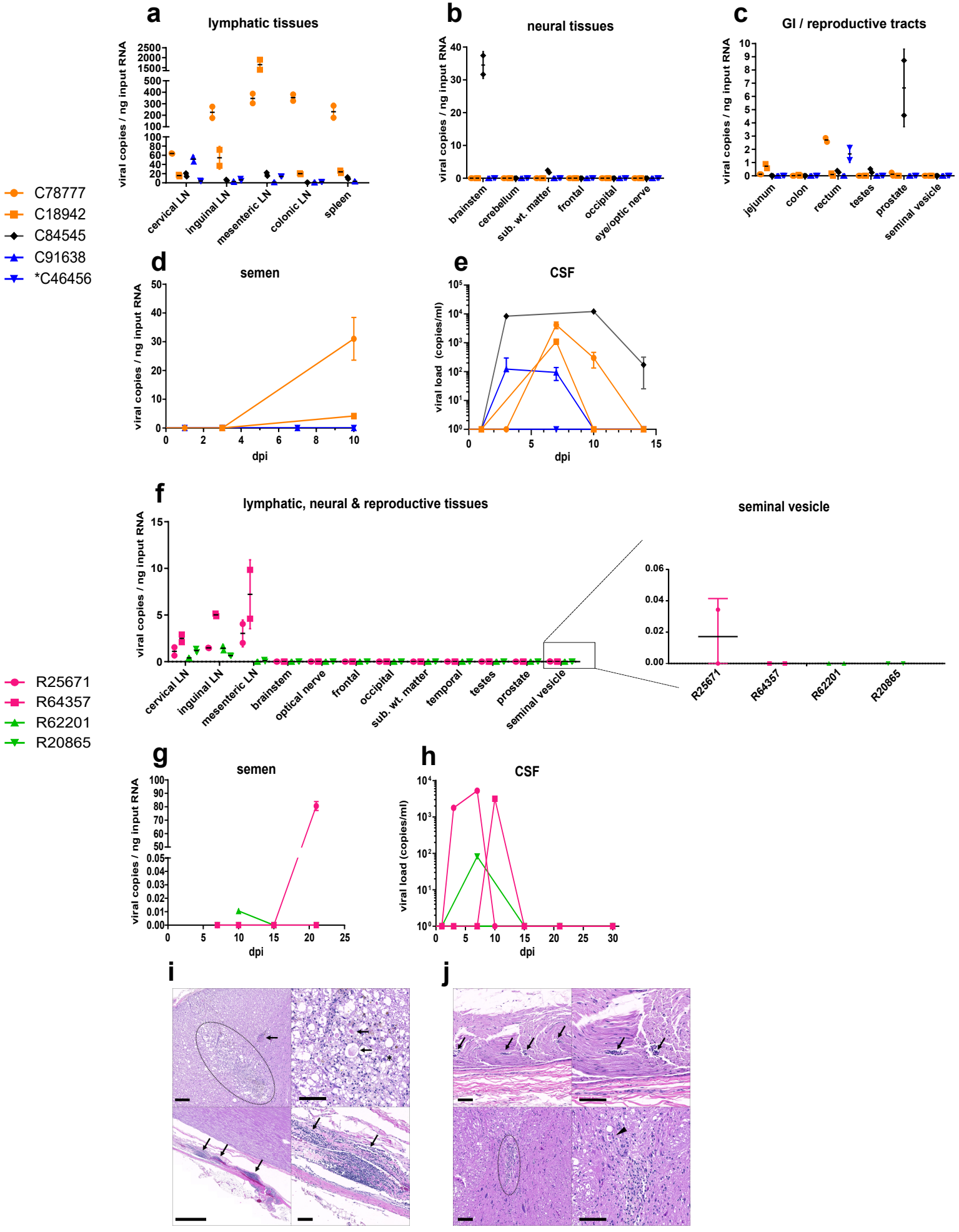
Fig 5: Enhanced tissue dissemination and neuropathology